Proceedings of the ASME 2023 18th International Manufacturing Science and Engineering Conference
MSEC2023
June 12-16, 2023, New Brunswick, New Jersey

MSEC2023-101622

FLAW DETECTION IN WIRE ARC ADDITIVE MANUFACUTRING USING IN-SITU ACOUSTIC SENSING AND GRAPH SIGNAL ANALYSIS

Benjamin Bevans
Virginia Tech
Blacksburg, VA

Andre Ramalho
UNIDEMI
Lisbon, Portugal

Ziyad Smoqi
UNL
Lincoln, NE

Aniruddha Gaikwad
UNL
Lincoln, NE

Telmo G. Santos
UNIDEMI
Lisbon, Portugal

Prahalada Rao
Virginia Tech
Blacksburg, VA

J.P. Oliveira
UNIDEMI
Lisbon, Portugal

ABSTRACT

The goal of this work is to detect flaw formation in wire arc additive manufacturing (WAAM). This process uses an electric arc as the energy source in order to melt metallic wire and deposit the new material, similar to metal inert gas (MIG) welding. Industry has been slow to adopt WAAM due to the lack of process consistency and reliability. The WAAM process is susceptible to a multitude of stochastic disturbances that cause instability in the electric arc. These arc instabilities eventually lead to flaw formation such as porosity, spatter, and excessive deviations in the desired geometry. Therefore, the objective of this work is to detect flaw formation using in-situ acoustic (sound) data from a microphone installed near the electric arc. This data was processed using a novel wavelet integrated graph theory approach. This approach detected the onset of multiple types of flaw formations with a false alarm rate of less than 2%. Using this method, this work demonstrates the potential for in-situ monitoring and flaw detection of the WAAM process in a computationally tractable manner.

Keywords: Rapid Prototyping and Solid Freeform Fabrication, Welding and Joining, Control and Automation.

1. INTRODUCTION

The objective of this work is to detect the onset of flaw formation during the wire arc additive manufacturing (WAAM) process using sensor data acquired in-situ. This is a first vital step towards quality control in the WAAM process to ensure functionality and minimize the amount of post process characterization that is needed to be done.

The WAAM process is classified under the directed energy deposition (DED) family of additive manufacturing (AM) process. In DED material is fed into the path of a energy source to fuse the new material to a previously existing layer [1]. Material being fed into the process can take the form of powder (P-DED) or wire (W-DED). The WAAM process used in this work falls under the W-DED processes since it uses a wire feed stock (Figure 1) [2]. WAAM can also be compared to metal inert/active gas (MIG/MAG) welding, in which there is an electric arc, protected by a shielding gas, that melts and deposits the wire feedstock material [3].

In WAAM, the welding torch is translated in three dimensions to produce a free-form geometry. The shielding gas is an inert gas (e.g., Argon, Nitrogen) that protects the electric arc from atmospheric oxygen and disturbances. If the electric arc is disturbed, the arc can become unstable and lead to flaw formation. Popular materials for WAAM include aluminum, titanium, mild steel, and stainless steel (this work) [4].

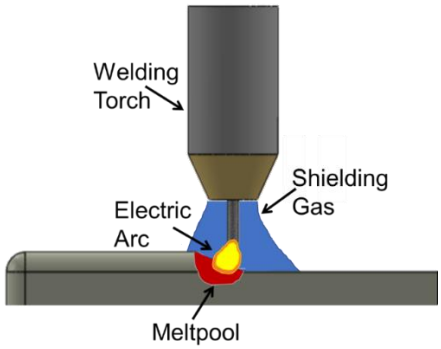

FIGURE 1: SCHEMATIC OF THE WIRE ARC ADDITIVE MANUFACTURING (WAAM) PROCESS. A WELDING HEAD DEPOSITS MATERIAL VIA THE USE OF A CONSUMABLE ELECTRODE BEING MELTED WITH AN ELECTRIC ARC.

A reason for the extensive interest in WAAM is its distinct cost advantages. The cost of welding wire is traditionally cheap, approximately $10/kg for mild steel. This is significantly less than the P-DED processes in which the metallic powder can cost over $100/kg. There is also a distinct volumetric throughput

advantage of the WAAM process over the other AM processes. WAAM can deposit material at a rate of ~50 $mm^3 \cdot s^{-1}$, which is over 10 times faster than P-DED processes which has an average deposition rate of 4 $mm^3 \cdot s^{-1}$ [4, 5]. This is a magnitude increase in volumetric deposition rate, as laser powder bed fusion (LPBF) generally fuses material ~10 times slower than P-DED.

The high volumetric deposition rate of WAAM is apt for manufacture of volumetrically large parts. The WAAM process has been integrated with one or more robots working together to produce these volumetrically large parts. This enables the additive manufacturing of parts such as wind turbines, excavators, oil drilling equipment, and even rocket bodies within hours as opposed to the weeks it would require with P-DED [6].

Industry has been slow to fully adopt the WAAM process due to its tendency to generate flaws such as porosity, warpage, and poor geometric accuracy [7]. These flaws are generally generated from either: poor selection of processing parameters, improper design of the part, sub-standard materials, or disruption of the arc (arc instability). Arc instabilities can be caused due to machine faults and stochastic disturbance from the environment, such as interference from contaminants. Since WAAM is being implemented in non-controlled environments, contaminants are a unique challenge that WAAM must address. This work will focus on the detection of arc instability. We note that even if there are no contaminants in the environment, a flaw formation will generally be accompanied by an unstable arc.

To illustrate the types of flaw generated in the WAAM process, Figure 2 shows X-ray computed tomography (XCT) slices of various layers in the samples produced in this work using stainless steel 316L. By observing these example slices porosity, line width deviations (geometric deviations), and contamination-based voids can be found. The voids in Figure 2 are correlated to disruption of the arc due to the presence of contaminants, as previously shown by Ramalho *et al.* [8].

FIGURE 2: EXAMPLE OF THE THREE MAJOR FLAWS OBSERVED IN THIS WORK: POROSITY, DEVIATION IN GEOMETRY OF AN INDIVIDUAL TRACKS (LINE WIDTH VARIATION), AND VOIDS DUE TO CONTAMINATION FROM THE SURROUNDING ENVIRONMENT.

2. MATERIALS AND METHODS

2.1 Experimental Setup

This work used 1 mm diameter AISI 316L stainless steel feedstock welding wire to produce three thin wall geometries. Each thin wall sample is 120 mm long and consists of 11 layers ($1.3mm \cdot layer^{-1}$), producing a part that is 14.5 mm tall and 4 mm wide. Material is deposited using a Kempi Pro MIG 3200 welding torch with Argon shielding gas. The process was controlled with the Kempi Pro MIG 401 wielding unit integrated into a custom-build CNC setup. To produce the parts, the welding torch moved at a rate of 300 $mm \cdot min^{-1}$ with a standoff distance of 8 mm in a bi-directional manner. The voltage of the electric arc was set at 20 V and the feedstock wire was extruded at a rate of 4 $m \cdot min^{-1}$.

Each thin wall sample had a different type of contaminant placed on layer 7 and 11 at 40 mm intervals, visualized in Figure 3 with red circles. Sample 1 used powdered chalk, sample 2 used oil, and sample 3 used sand as their respective contaminant. These contaminants were added by drilling a flat-bottom hole of ϕ2.5 mm × 1 mm. In this work, three types of common shop floor contaminants (chalk, oil, and sand) were placed in controlled, and systematic, locations so that the subsequent arc instability can be monitored using in-situ acoustic data. Since the WAAM process is generally performed in a shop floor environment, various contaminants can enter and destabilize the electric arc.

To monitor this process in-situ, a Shure SM57 acoustic microphone was attached to the welding torch to maintain a distance of 20 cm from the welding torch, at a nominal angle of 20°, shown in Figure 3. This allowed for the microphone to always be a constant distance from the electric arc, i.e. the meltpool (material deposition point). Data was collected at a rate of 25.6 kHz.

After the parts were produced, post process non-destructive testing in the form of XCT was performed on all three samples. A Nikon XTH 255 ST system was used to collect data at a resolution of 17 µm/voxel. The data was subsequently processed using the native volume graphics software.

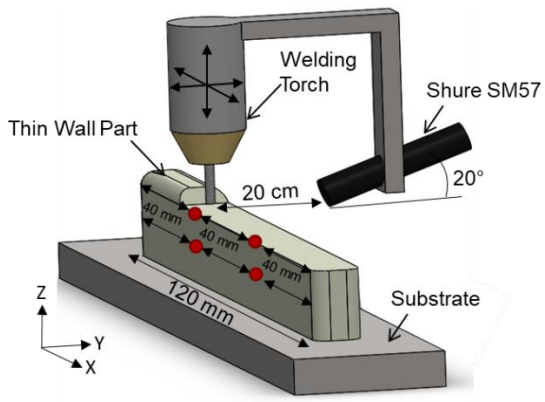

FIGURE 3: PICTURE AND SCHEMATIC OF THE EXPERIMENTAL SET-UP. A SHURE SM57 ACOUSTIC SENSOR IS ATTACHED TO THE WELDING TORCH MAINTAINING A CONSTANT DISTANCE TO THE ELECTRIC ARC.

2.2 Effect of Contaminants on the Electric Arc

In this work, arc instability conditions caused by three different types of contaminants, viz., chalk, oil, and sand, were analyzed and detected. These contaminants are commonly found on the shop floor. The following phenomena are observed based on the sensor signal and the physical part produced.

In the example XCT slice of sample 1 shown in Figure 4(a2) there are prominent line width variations at the point where the chalk contamination was placed (purple). Due to the relatively low packing density of chalk (910-960 $kg \cdot m^{-3}$ [9]), the chalk was blown out of its hole by the argon shielding gas. The aerosolized powder then disrupted the shielding gas, causing the electric arc to dissipate, thus leading to less material deposition at these points. The phenomena is visualized in Figure 4(a1).

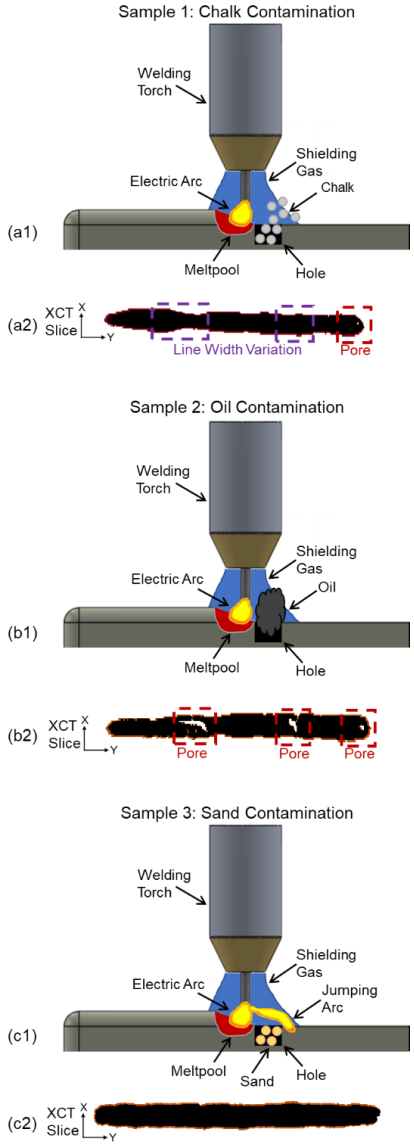

FIGURE 4: (A) EFFECT OF CHALK CONTAMINATION, (B) EFFECT OF THE OIL CONTAMINATION, (C) EFFECT OF THE SAND CONTAMINATION. CONTAMINATION ZONES ARE MARKED IN GREEN.

In the example XCT slice of sample 2, Figure 4(b2), there are large pores, classified as voids, at the locations where the oil contamination was introduced (red). These voids were likely generated due to the electric arc, generating temperatures in excess of 1450 °C, vaporizing the oil which has a relatively low boiling temperature (300 °C) [10]. The vaporized oil disrupts the shielding gas, thus suppressing the continuity of the electric arc and interrupting material deposition, depicted in Figure 4(b1). This explanation is supported by the excessive amount of spatter particles found on sample 2 (Figure 9).

In the XCT slice of sample 3, Figure 4(c2), there are minimal flaws observed. Due to the lack of physical defects in this sample, the electric arc was not disrupted, as observed in sample 1 and 2. This would imply that the electric arc was able to transition across the hole in which the sand contaminant was placed in and not generate excessive defects, depicted in Figure 4(c1). This is supported by the high packing density of sand of approximately 1,300 $kg \cdot m^{-3}$ compared to chalk [11].

Another insight from this work is that flaws generated in the WAAM process are not isolated incidents. Flaws generated on a layer, if significant enough, can force an arc instability on subsequent layers, thus generating new flaws, depicted in Figure 5. For example, if there is a void on layer n, then on layer $n+1$ the standoff distance will change. This change in the standoff distance can propagate flaws in two ways; (1) weakening the electric arc, thereby, affecting material deposition, and (2) requiring more material to be deposited to fill the excess gap in the layer.

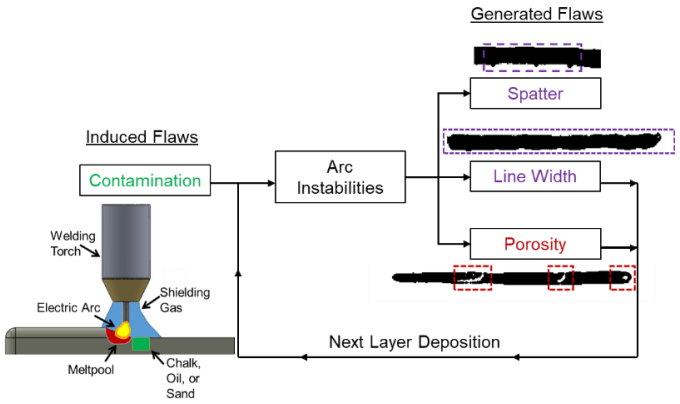

FIGURE 5: FLOW CHART DIAGRAM DEPICTING HOW ARC INSTABILITIES CAN CREATE FLAWS, AND THOSE FLAWS CAN SUBSEQUENTLY PRODUCE NEW ARC INSTABILITIES.

2.3 Signal Processing using Wavelets & Graph Theory

In this work, the signal analysis approach consists of three basic steps visualized in Figure 6. The following three steps discussed in detail herewith were performed:

(1) Signal Filtering: The raw data acquired by the acoustic sensor is filtered using wavelet analysis to remove background process noise [12].
(2) Signal Processing (Analysis): The filtered sensor data is analyzed using spectral graph theory approach to extract the Laplacian Fiedler number (λ_2) [13].
(3) Process Monitoring: The Fiedler number (λ_2) is tracked in an exponentially weighted moving average (EWMA) control chart [14].

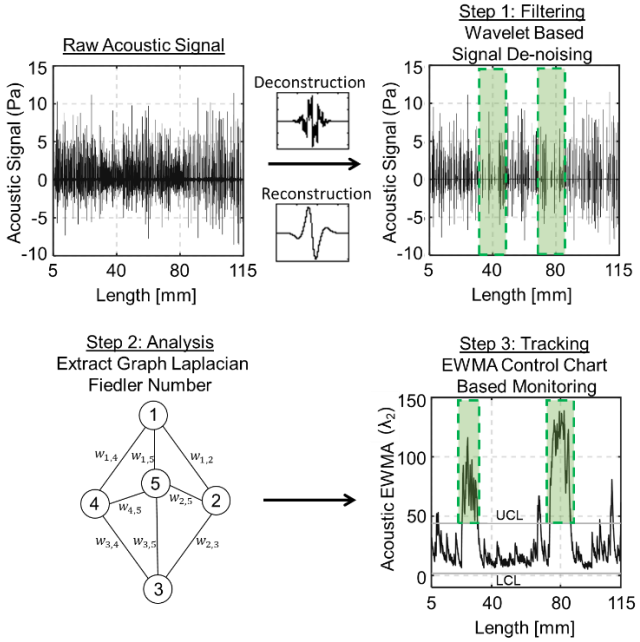

FIGURE 6: OVERVIEW OF THE APPROACH USED FOR FLAW DETECTION. (1) THE FIRST STEP IS FILTERING OUT THE NOISE USING WAVELET ANALYSIS. (2) NEXT GRAPH THEORY ANALYSIS IS USED TO EXTRACT PROCESS SIGNATURES (FIEDLER NUMBER). (3) THE FIEDLER NUMBER IS THEN TRACKED USING AN EWMA CONTROL CHART.

Step 1 – Wavelet Filtering

Wavelet transform decomposition is used to remove the background noise from the machine and the environment [12]. The wavelet transform can be compared to the Fourier transform where the signal is decomposed into its base frequencies. However, unlike the Fourier transform the wavelet transform allows the data to be analyzed in both the frequency and time domains simultaneously. Using this method, the exact location of undesired signal frequencies can be identified, which then can be correlated to arc instability-based flaw formation.

Another difference between the Fourier and wavelet transforms is that the wavelet transform has many functional bases to perform the decomposition, as opposed to only sinusoidal bases. The basis for the wavelet transform are called wavelets. If needed, custom wavelets can be made and used to decompose the signal. Another distinct advantage over the Fourier transform is that the wavelet transform accommodates non-stationary data sets with sharp discontinuities in the original signal [15]. Because the acoustic data in this work is replete with sharp discontinuities corresponding to arc instabilities, the use of wavelet transforms is vital for this work.

To ease data processing, the discrete wavelet transforms (DWT) is used to decompose the raw acoustic signal (S). This formulation shown in Eqn.(1) and is derived from the continuous wavelet transform (CWT) [15].

$$W(2^i, 2^i n) \triangleq \frac{1}{\sqrt{2^i}} \sum_{d=1}^{d=N} \bar{\psi}\left(\frac{d}{2^i} - n\right) S(d) \qquad (1)$$

In this equation the analyzing wavelet function is denoted with $\bar{\psi}$. The variable d is the discrete data point in the signal (S), containing N total data points. The function 2^i indicates the discrete values of the time dilation and translation at the frequency level (octave) i. For this work, n=1 so that both the time translation and dilation are changed at the same interval, this is standard for basic wavelet analysis [16]. The DWT is used to deconstruct the signal into its base frequencies (octaves). To successfully decompose the acoustic data in this work, a biorthogonal 3.3 wavelet is used to decompose the raw signal into eight discrete octaves (i=1,2,3,4,5,6,7,8).

Once the signal is decomposed into discrete octaves, hard limit thresholding is used to remove the background noise at each octave. The threshold limit for each octave is found heuristically by comparing each octave to layer 7 of sample 1. This allows for each octave to be compared to a training condition of chalk contamination and its effect on the acoustic signal. Once the thresholds are determined, they are not changed under the different parts and layers.

Once each octave has been de-noised, the discrete inverse wavelet transforms (DIWT) is performed to convolve each octave together into a reconstructed de-noised signal (S_d). This process uses the biorthogonal 3.3 reconstruction wavelet. The result of de-noising an example layer of acoustic data can be seen in step 1 of Figure 6. Notice that at the 40- and 80- mm points (where chalk contamination is placed; highlighted in green) in the de-noised signal, the signal dissipates indicating a weaker arc. This is not noticed in the raw acoustic signal.

Step 2 – Signal Analysis

In this step, the de-noised acoustic signal (S_d) is processed using spectral graph theory. This allows for the acoustic data to be analyzed in the graph space to extract the Fiedler number (λ_2), which is used as the monitoring statistic. The Fidler number is chosen as the monitoring statistic as it is a singular number that expresses the overall connectivity of the inputted data. Since the de-noised acoustic signal depicts changes in signal strength at arc instabilities, the Fielder number is able to detect this change in connectivity.

After wavelet filtering, the de-noised acoustic signal (S_d) is analyzed in the graph domain, and a single number called the Fiedler number (λ_2) is obtained. The Fiedler number is then used as the monitoring statistic for detecting flaw formation. This approach circumvents the extraction of several statistical features from the sensor data for process monitoring, and is therefore computationally efficient. The mathematical properties of the Fiedler number are described in depth in Ref. [14].

To extract multiple Fiedler number per layer of acoustic data, the de-noised signal is divided into 1200 windows per layer, where each window contains 512 discrete data points. For a physical representation of this process, each window represents 0.1 mm of welding torch travel, over 0.02 seconds. This results in 10 windows per mm of travel.

For each window, the Fiedler number (λ_2, the monitoring statistic) is extracted, resulting in a total of 1200 Fiedler numbers per layer. The specific process of obtaining the Fiedler number is detailed Tootooni *et. al.* [13]. A brief description of the process used in this work is detailed in the following steps.

First, for each window, the 512 data points are used to create a weighted adjacency matrix (*w)* to determine the Euclidean distance of each data point to every other data point. For the 1-D de-noised acoustic signal, this formulation can be shown as:

$$w(i,j) = |S_d(i) - S_d(j)| \tag{2}$$

The next step is to generate a normalized Laplacian matrix to extract the Fiedler number. Accordingly, the calculated weighted adjacency matrix is converted into binary form (0's and 1's) using ε as the thresholding value. Values larger than ε are converted to a one, and the rest are converted to zeros. This binary form of the weighted adjacency matrix is called the sparse adjacency matrix (*H).*

Since each window is not a purely isolated data set, meaning that in the physical system the acoustic signal from the previous window can be correlated to the current window, and therefore, affect the current window, the thresholding value ε is not a constant value in this work. The calculated value ε is the average value of the weighted adjacency matrix from the current window and the previous 5 windows. This allows for the acoustic data from the previous 0.5 mm to be considered when determining the thresholding value ε.

From the sparse adjacency matrix (*H*) the normalized Laplacian matrix $\mathcal{L}$ can be calculated for the window [17]:

$$\mathcal{L} = D - H \tag{3}$$

In this formulation, *D* is the degree matrix, viz., the diagonal sum of the sparse adjacency matrix. From this Laplacian matrix, the eigenvalues (λ) and eigenvectors (ν) are extracted for each window *k* using the following equation [17]:

$$\mathcal{L}\nu = \lambda\nu \tag{4}$$

The second eigenvalue (λ_2) and eigenvector (ν_2) are called the Fiedler number (λ_2) and Fiedler vector (ν_2) respectively. As stated previously, the Fiedler number is a singular value that expresses the overall connectivity of the inputted data. Essentially, the Fiedler number monitoring statistic tracks the change in connectivity over the 1200 windows in a given layer. To monitor and detect the change in this Fiedler number between each window *k*, an exponentially weighted average (EWMA) control chart is used [18].

Step 3 – Process Monitoring (Tracking)

An EWMA chart detects anomalies by tracking a monitoring statistic, if this statistic exceeds a certain threshold it is deemed out of control (anomaly). For this work the EWMA monitoring statistic Z_k for a window k is a function of the Fiedler number $\lambda_{2,k}$ for window k.

$$Z_k = \alpha\lambda_{2,k} + (1-\alpha)Z_{k-1} \tag{5}$$

This EWMA statistic weights the incoming data point ($\lambda_{2,k}$, Fiedler number of window k) to the previous EWMA statistic, by using a weight (α). In traditional works, the weight (α) is between 0.1-0.3, thus weighing (trusting) the latest incoming data point less than the previous [18]. This makes the EWMA statistic (*Z*) slow to change, it changes significantly if there are multiple. consecutive data points changing in a similar manner. This minimizes the effect of noise from outlier data points. In this work, $\alpha = 0.1$ to account for the high degree of stochastic fluctuation in the data.

To find the control limits in this work, the flaw free condition found in layers 8 and 9 of sample 3 are used. The threshold of the upper control limit (UCL) and lower control limit (LCL) should be placed just above the nominal fluctuations of the nominal (flaw free) data used to calibrate. To find these limits the following equation is used where μ_0 and σ_0 are the average and standard deviation of the data set respectively [14]:

$$\text{UCL, LCL} = \mu_0 \pm \tau * \sigma_0\sqrt{\frac{\alpha}{2-\alpha}} \tag{6}$$

The value of τ represents the number of standard deviations needed to account for where the outliers occur. In traditional control charts τ = 3, however, due to the stochastic, non-stationary, and non-linear nature of the acoustic data used in this work the value τ =10 [19]. This resulted with an UCL and LCL of 44 and 1.5 respectively. An example of these setting in practice can be found in step 3 of Figure 6. Notice that near the 40- and 80- mm points there are clear spikes above the control limit where the chalk contamination is placed.

These setting resulted in an average run length (ARL_0) of 62 and a false alarm rate of 1.6% [20]. Evaluation metrics were extracted from the flaw free conditions on layer 8 and 9 of sample 3. This result is on par with the false alarm rates in both DED [21] and LPBF [22, 23] flaw detection research.

3. RESULTS AND DISCUSSION

3.1 Flaw Detection at the Layer Level

Shown in Figure 7, is an example of the proposed method in practice on layer 11 of sample 1 which had 2 chalk contaminations in green. In the XCT slice (Figure 7(a)) there is a line width variation at the start of the layer (purple), then another line width variation at the contamination points (green), and a pore at the end of the layer (red). All four of these defects are noted in EWMA control chart shown in Figure 7(b), where all the flaw-prone regions show a clear spike above the upper control limit. These spikes above the control limit indicate an arc instability that generated the respective flaw.

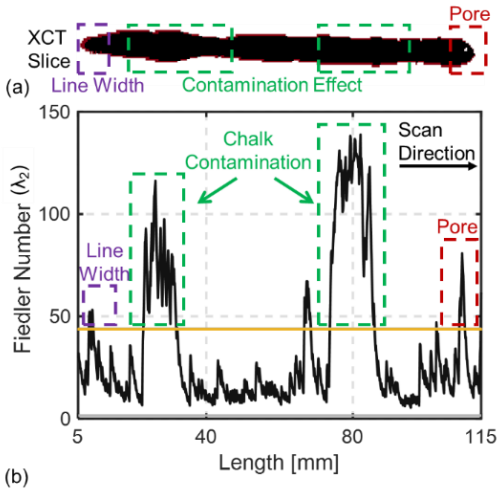

FIGURE 7: (A) LINE WIDTH VARIATIONS ARE APPARENT IN THE XCT SLICE OF THIS LAYER. (B) LINE WIDTH VARIATION CAUSED BY CONTAMINATION (GREEN) CROSSES THE UPPER CONTROL LIMIT IN THE EWMA CONTROL CHART.

Another example of the proposed method is seen in Figure 8, which shows data from layer 11 of sample 2, which contains two oil contamination zones. In Figure 8(a) there is a line width variation at the start of the layer and two pinch points later on in the build demarcated in purple. There are also 2 large voids in the sample at the 40- and 80-mm point where the oil contamination was placed (red), and a final pore at the end of the layer. All of these flaws show a clear spike above the control limit in Figure 8(b).

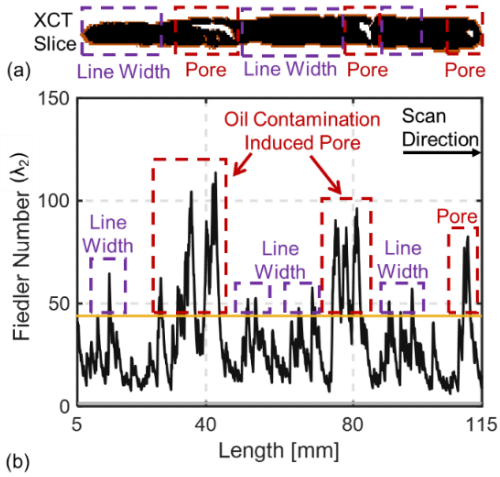

FIGURE 8: (A) TWO VOIDS CAUSED BY CONTAMINATION (RED), LINE WIDTH VARIATION (PURPLE), AND POROSITY (RED) ARE SEEN IN THE XCT SLICE OF THIS LAYER. (B) ALL OF THESE FLAWS ARE ACCURATELY DETECTED IN THE CONTROL CHART.

This indicates that the method accurately detects arc instability-based flaws across multiple samples with appreciable spatial resolution. The model is able to detect the location of arc instabilities that can lead to flaw formation, however, it is currently unable to determine what type of flaw if generated as a result of the arc instability.

3.2 Part Level Detection

To obtain a holistic view of the porosity on a part level, the total number of arc instabilities found in each sample is summed and compared to the other samples. Sample 1 which contained the chalk contaminant, shown in Figure 9, has 1,001 total arc instability detections throughout the sample. Layers 7 and 11, which contained contaminations are demarcated in green, porosity is demarcated in red, and line width variations are demarcated in purple. This sample contains five large pores and a significant number of line width, including a phenomenon called walk off at the edges of the sample.

In comparison, sample 2 contained six large pores, line width variations, and a large amount of spatter (satellite) particles on the side of the sample. Sample 2 had a total of 1,991 arc instability detections throughout the sample that correlate to the unstable meltpool generating spatter and large pores.

Finally, sample 3 only had three small pores and minimal line width variations. The total number of arc instability in this sample is 343 which correlates to the more stable meltpool generating the higher quality part.

This indicates that this method is able to determine the overall quality of WAAM produced parts by counting the total number or arc instability detections in the sample.

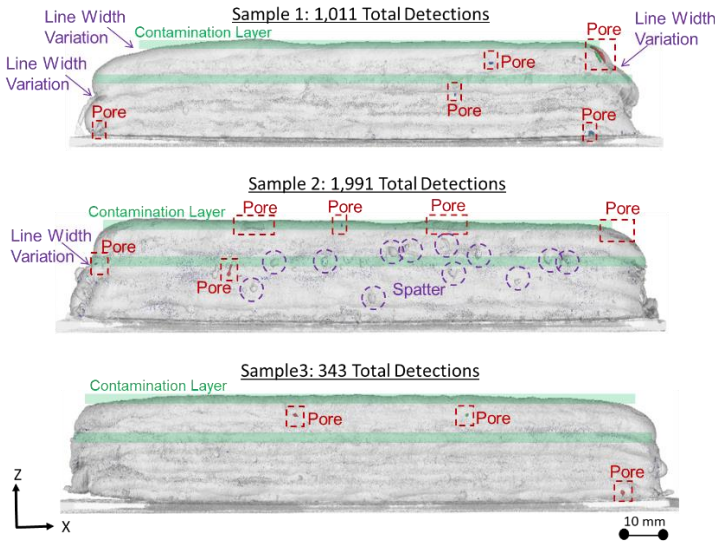

FIGURE 9: COMPARISON BETWEEN ALL THREE SAMPLES AND THE NUMBER OF ARC INSTABILITY DETECTIONS IN EACH LAYER. SAMPLE 3 HAD BOTH THE FEWEST NUMBER OF ARC DETECTIONS AND THE FEWEST FLAWS. IN COMPARISON TO SAMPLE 1 AND SAMPLE 2 WHICH HAD OVER 1,000 DETECTIONS AND SIGNIFICANT NUMBERS OF FLAWS OBSERVED.

4. CONCLUSION

This work developed and applied a wavelet-based graph theory signal analysis approach for flaw detection in the WAAM process. In-situ acoustic microphone signals were de-noised using a wavelet transform, and analyzed using spectral graph theory to extract a statistic called the Fiedler number. This Fiedler number was then tracked in an exponentially weighted moving average (EWMA) control chart to monitor and detect when an unstable arc occurred that will lead to flaw formations. The effectiveness of the approach was demonstrated in the context of detecting various arc instabilities in the WAAM process. The approach is evaluated to have a false alarm rate of less than 2%.

This work is an important first step to the in-situ part qualification of WAAM parts and for future closed-loop control algorithms. Future work will entail not only detecting arc instability but also type of flaw formation via the use of machine learning algorithms. Additionally, closed-loop control algorithms will be developed to detect when an excessive amount of flaw formation exists and remove the layer using CNC milling. This layer can then be re-deposited under different settings. Finally, this method will be tuned to work with other materials on various WAAM machines.

ACKNOWLEDGEMENTS

Andrè Ramalho acknowledges Fundação para a Ciência e a Tecnologia (FCT-MCTES) for funding the Ph.D. Grant UI/BD/151018/2021. André Ramalho, Telmo G. Santos and J.P. Oliveira acknowledge Fundação para a Ciência e a Tecnologia (FCT-MCTES) for its financial support via the project UID/00667/2020 (UNIDEMI). JPO acknowledges the funding of CENIMAT/i3N by national funds through the FCT-Fundação para a Ciência e a Tecnologia, I.P., within the scope of Multiannual Financing of R&D Units, reference UIDB/50025/2020-2023. This activity has received funding from the European Institute of Innovation and Technology (EIT) – Project Smart WAAM: Microstructural Engineering and Integrated Non-Destructive Testing.

Prahalada Rao acknowledges funding from the Department of Energy (DOE), Office of Science, under Grant number DE-SC0021136, and the National Science Foundation (NSF) [Grant numbers CMMI-1719388, CMMI-1920245, CMMI-1739696, CMMI-1752069, PFI-TT 2044710, ECCS 2020246] for funding his research program. This work espousing the concept of online process monitoring in WAAM was funded through the foregoing DOE Grant (Program Officer: Timothy Fitzsimmons), which supported the doctoral graduate work of Mr. Benjamin Bevans. The XCT work was performed at the Nebraska Nanoscale Facility: National Nanotechnology Coordinated Infrastructure under award no. ECCS: 2025298, and with support from the Nebraska Research Initiative through the Nebraska Center for Materials and Nanoscience and the Nanoengineering Research Core Facility at the University of Nebraska-Lincoln.

REFERENCES

1. Dass, A. and A. Moridi, *State of the art in directed energy deposition: From additive manufacturing to materials design.* Coatings, 2019. **9**(7): p. 418-418.
2. Ahn, D.-G., *Directed Energy Deposition (DED) Process: State of the Art.* International Journal of Precision Engineering and Manufacturing-Green Technology, 2021. **8**(2): p. 703-742.
3. Xia, C., et al., *A review on wire arc additive manufacturing: Monitoring, control and a framework of automated system.* Journal of Manufacturing Systems, 2020. **57**: p. 31-45.
4. Singh, S.R. and P. Khanna, *Wire arc additive manufacturing (WAAM): A new process to shape engineering materials.* Materials Today: Proceedings, 2021. **44**: p. 118-128.
5. Ding, D., et al., *The well-distributed volumetric heat source model for numerical simulation of wire arc additive manufacturing process.* Materials Today Communications, 2021. **27**: p. 102430-102430.
6. Simunovic, S., et al. *Metal big area additive manufacturing: Process modeling and validation*.
7. Xu, F., et al., *Realisation of a multi-sensor framework for process monitoring of the wire arc additive manufacturing in producing Ti-6Al-4V parts.* International Journal of Computer Integrated Manufacturing, 2018. **31**(8): p. 785-798.
8. Ramalho, A., et al., *Effect of contaminations on the acoustic emissions during wire and arc additive manufacturing of 316L stainless steel.* Additive Manufacturing, 2022. **51**: p. 102585-102585.

9. Trypuć, M. and K. Białowicz, *CaCO3 production using liquid waste from Solvay method.* Journal of Cleaner Production, 2011. **19**(6-7): p. 751-756.
10. Wu, B., et al., *Organochlorine Compounds with a Low Boiling Point in Desalted Crude Oil: Identification and Conversion.* Energy & Fuels, 2018. **32**(6): p. 6475-6481.
11. Osunbitan, J.A., D.J. Oyedele, and K.O. Adekalu, *Tillage effects on bulk density, hydraulic conductivity and strength of a loamy sand soil in southwestern Nigeria.* Soil and Tillage Research, 2005. **82**(1): p. 57-64.
12. Yansun Xu, J.B.W.D.M.H. and L. Jian, *Wavelet transform domain filters: a spatially selective noise filtration technique.* IEEE Transactions on Image Processing, 1994. **3**(6): p. 747-758.
13. Tootooni, M.S., et al., *A Spectral Graph Theoretic Approach for Monitoring Multivariate Time Series Data From Complex Dynamical Processes.* IEEE Transactions on Automation Science and Engineering, 2018. **15**(1): p. 127-144.
14. de Vargas, V.d.C.C., L.F. Dias Lopes, and A. Mendonça Souza, *Comparative study of the performance of the CuSum and EWMA control charts.* Computers & Industrial Engineering, 2004. **46**(4): p. 707-724.
15. Shensa, M.J., *The discrete wavelet transform: wedding the a trous and Mallat algorithms.* IEEE Transactions on signal processing, 1992. **40**(10): p. 2464-2482.
16. Daubechies, I., *The wavelet transform, time-frequency localization and signal analysis*. 2009: Princeton University Press.
17. Chung, F., *Chapter 1. Eigenvalues and the Laplacian of a graph.* Spectral Graph Theory, 1997: p. 1-22.
18. Borror, C.M., D.C. Montgomery, and G.C. Runger, *Robustness of the EWMA Control Chart to Non-Normality.* Journal of Quality Technology, 1999. **31**(3): p. 309-316.
19. MacGregor, J.F. and T.J. Harris, *[Exponentially Weighted Moving Average Control Schemes: Properties and Enhancements]: Discussion.* Technometrics, 1990. **32**(1): p. 23-26.
20. Li, Z., et al., *The computation of average run length and average time to signal: an overview.* Journal of Statistical Computation and Simulation, 2014. **84**(8): p. 1779-1802.
21. Zhao, X., et al. *Automated Anomaly Detection of Laser-Based Additive Manufacturing Using Melt Pool Sparse Representation and Unsupervised Learning*. University of Texas at Austin.
22. Imani, F., et al., *Process Mapping and In-Process Monitoring of Porosity in Laser Powder Bed Fusion Using Layerwise Optical Imaging.* Journal of Manufacturing Science and Engineering, 2018. **140**(10): p. 101009-101009-14.
23. Smoqi, Z., et al., *Monitoring and prediction of porosity in laser powder bed fusion using physics-informed meltpool signatures and machine learning.* Journal of Materials Processing Technology, 2022. **304**: p. 117550.